

Efficient Receptive Field Tiling in Primate V1

Highlights

- Spatial frequency and ocular dominance maps have parallel gradients in macaque V1
- Map regions encoding higher spatial frequencies align with binocular zones
- Retinotopy is extremely precise when zooming into the maps with two-photon imaging
- Smooth micro-retinotopy requires efficient alignment of feature maps for full coverage

Authors

Ian Nauhaus, Kristina J. Nielsen,
Edward M. Callaway

Correspondence

nauhaus@austin.utexas.edu (I.N.),
callaway@salk.edu (E.M.C.)

In Brief

Nauhaus et al. used two-photon imaging in macaque V1 to reveal a precise and efficient functional architecture. They first show that compartments of high spatial frequency lie within binocular zones. Then they demonstrate unexpectedly smooth progression of receptive field location.

Efficient Receptive Field Tiling in Primate V1

Ian Nauhaus,^{1,2,3,*} Kristina J. Nielsen,^{1,2,4} and Edward M. Callaway^{1,*}

¹Systems Neurobiology Laboratories, The Salk Institute for Biological Studies, La Jolla, CA 92037, USA

²Co-first author

³Present address: Center for Perceptual Systems, Department of Psychology, University of Texas at Austin, 108 East Dean Keeton, Stop A8000, Austin, TX 78712, USA

⁴Present address: Zanvyl Krieger Mind/Brain Institute, Department of Neuroscience, Johns Hopkins University, 3400 North Charles Street, Baltimore, MD 21218, USA

*Correspondence: nauhaus@austin.utexas.edu (I.N.), callaway@salk.edu (E.M.C.)

<http://dx.doi.org/10.1016/j.neuron.2016.07.015>

SUMMARY

The primary visual cortex (V1) encodes a diverse set of visual features, including orientation, ocular dominance (OD), and spatial frequency (SF), whose joint organization must be precisely structured to optimize coverage within the retinotopic map. Prior experiments have only identified efficient coverage based on orthogonal maps. Here we used two-photon calcium imaging to reveal an alternative arrangement for OD and SF maps in macaque V1; their gradients run parallel but with unique spatial periods, whereby low-SF regions coincide with monocular regions. Next we mapped receptive fields and found surprisingly precise micro-retinotopy that yields a smaller point-image and requires more efficient inter-map geometry, thus underscoring the significance of map relationships. While smooth retinotopy is constraining, studies suggest that it improves both wiring economy and the V1 population code read downstream. Altogether, these data indicate that connectivity within V1 is finely tuned and precise at the level of individual neurons.

INTRODUCTION

The sensory cortex of large mammals is organized into continuous maps, whereby adjacent neurons encode similar features and locations of the environment (Mountcastle et al., 1955). Although the benefits and mechanisms leading to this scheme are still debated (Chklovskii and Koulakov, 2004; Horton and Adams, 2005; Nauhaus and Nielsen, 2014), it is certain that functional continuity comes at a cost of reduced feature coverage that can be minimized by specific patterns of organization (Swindale, 1991; Swindale et al., 2000). For instance, the Hubel and Wiesel (1974) ice-cube model demonstrates how orthogonal alignment between the gradients of orientation and ocular dominance (OD) maps can yield a full representation of two parameters for each retinotopic location. Many studies have since validated the general notion that V1 maps can be efficiently combined via orthogonal gradients (Bartfeld and Grinvald, 1992;

Hübener et al., 1997; Issa et al., 2000; Nauhaus et al., 2012; Obermayer and Blasdel, 1993; Yu et al., 2005), with those in the macaque having the strictest orthogonality between maps of orientation and OD and between maps of orientation and spatial frequency (SF). However, it is still uncertain how all three of the known periodic maps are aligned in the macaque. Furthermore, it is unclear how the cell-by-cell maps of receptive field (RF) location (i.e., the micro-retinotopy) tile the visual field within compartments of the periodic maps, yet this knowledge is required for a complete assessment of how the V1 functional architecture affects coding.

The micro-retinotopy helps define the V1 point-image, which is the cortical area devoted to processing a point of visual space. The size of the point-image increases with the SD, or scatter, in RF position for a finite point in the cortex. If retinotopy remains perfectly smooth as we zoom into the map, then scatter equals zero. Some electrode studies in the primate have yielded a substantial degree of scatter (Hubel and Wiesel, 1974), whereas newer studies in the cat using more advanced electrodes and quantification have identified far less scatter (Hetherington and Swindale, 1999; Jin et al., 2011). Hubel and Wiesel estimated that the amount of scatter in primate V1 is comparable to RF size at a given eccentricity, which would double the area of the point-image relative to the baseline of zero scatter. More scatter in the retinotopic map would greatly relax restrictions placed on inter-map geometry for achieving feature coverage. In addition to scatter, local distortions may reside within the retinotopic map. One proposition is that large shifts in RF location coincide with local discontinuities in the orientation map (Das and Gilbert, 1999). An interdependence of this form would hamper coding efficiency, as a given point-image would be biased to cover a limited range of orientations. However, this result is disputed by other studies showing orientation and retinotopy maps to be independent (Bosking et al., 2002; Hetherington and Swindale, 1999).

Here we used two-photon calcium imaging to answer multiple fundamental questions about functional architecture in the macaque that are directly relevant to V1's coding capacity. In part 1, we used wide-field two-photon imaging to simultaneously map orientation, OD, and SF. Wide-field imaging was used to capture a full spatial period of these periodic maps. Similar to previous studies, we observed a strongly orthogonal relationship between orientation and OD maps (Bartfeld and Grinvald, 1992; Obermayer and Blasdel, 1993), as well as orientation and SF

maps (Nauhaus et al., 2012). To complete the picture of how these classic stimulus properties are mapped, we demonstrate that OD and SF maps have gradients that progress in parallel and that regions of low SF coincide with the center of OD columns. In other words, the maps have unique spatial periods, a valid strategy for achieving coverage (Swindale, 1991). This is in stark contrast to results in the carnivore suggesting that all three of the above-mentioned maps have near orthogonal alignment, at most locations.

In part 2 of this study, we examined the retinotopy down to the finest spatial scale in primate V1 by determining RF locations on a cell-by-cell basis across $\sim 200 \mu\text{m}$ of V1. The retinotopy in each region was observed as systematic shifts of the RF centers that were much smaller than the RF widths (i.e., minimal scatter), thus placing greater constraints on the alignment between functional maps. This highlights the significance of the observed detailed inter-map alignment seen in part 1. Furthermore, we found substantial independence between orientation-tuning curves that was uncorrelated with the minimal RF scatter, which should yield greater orientation discrimination at all visuotopic locations. In summary, our data show that primate V1 achieves efficient coverage of orientation, OD, and SF, using a combination of orthogonal and non-orthogonal gradients, and that it counterbalances smooth micro-retinotopy with efficient alignment of the three functional maps.

RESULTS

The Joint Organization of Orientation, OD, and SF Maps

Orientation, OD, and SF form continuous maps in primate V1. The orthogonal alignment between the orientation and the other two maps is well established in the primate (Bartfeld and Grinvald, 1992; Nauhaus et al., 2012; Obermayer and Blasdel, 1993), thus demonstrating an efficient alignment between two of the three map pairings. However, SF and OD maps cannot also be orthogonal at each location of the 2D surface. To complete the picture of how these three classic stimulus properties are mapped, we presented drifting gratings of different orientation and SF to either eye. Similar to our previous experiments, multiple injections of the calcium-sensitive dye Oregon Green BAPTA-1AM (OGB) were made to cover a field of view that spanned at least one spatial period ($>500 \mu\text{m}$) of the maps (Nauhaus et al., 2012). Using two-photon imaging of visual stimulus-evoked fluorescence changes, tuning curves for orientation, SF, and OD were generated for each pixel in each imaging region (Figure 1).

We first replicated the result that orientation maps are orthogonal to both OD (Bartfeld and Grinvald, 1992; Obermayer and Blasdel, 1993) and SF maps (Nauhaus et al., 2012) in macaque V1 (Figures 2A and 2B; Table 1). Next we performed the first direct comparison of SF and OD maps in macaque V1. We found that the two periodic maps were in phase such that regions of high SF (red patches in Figure 2C) coincided with transition zones in the OD map (i.e., binocular regions, indicated by thick lines in Figure 2C). We quantified this observation by computing the correlation coefficient between the binocularity map (binocularity map = $1 - |\text{OD map}|$) (Figure 2D) and the logarithm of the SF map. There was a positive correlation in five of six imaging

regions ($p < 10^{-10}$ in five of six regions and $p > 0.05$ in the remaining region; Table 1). This positive correlation implies that SF and binocularity maps have similar spatial periods. As the OD map had twice the spatial period as the binocularity map, it also implies that the OD map has a larger spatial scale than the SF map.

We quantified the spatial periods of OD and SF maps by computing the Fourier transform of their autocorrelation function (Figure 2E), i.e., we found the peak location of the power spectrum. Since most of the variance in the OD maps was contained along a single axis in each imaging region, perpendicular to the OD bands, the power spectrum in each imaging region was only computed along this axis. Furthermore, as we were interested in how the SF map gradients are interwoven with the parallel OD map gradients, the power spectrum of the SF map was computed along the same axis. In each imaging region, both maps produced a single peak in the power spectrum from which we determined the spatial period (Table 1). The average ratio of OD period to SF period across imaging regions was 1.42. Taken together, the data show that OD and SF maps have unique spatial periods and are aligned to make binocular regions encode the highest SFs.

This result closes a significant gap in our understanding of how stimulus features are jointly represented by cortical maps. A large angle of incidence between map gradients is the most commonly considered means of obtaining complete coverage, and it is the only form of interaction observed in other species where similar measurements have been made (Hübener et al., 1997; Issa et al., 2000; Yu et al., 2005). However, differences in spatial periods between maps also could be used to obtain coverage (Swindale, 1991). Indeed, our data demonstrate that maps in primate V1 exhibit orthogonally aligned map gradients, along with differences in periodicity. The level of intimacy among the three maps strongly suggests that they are built from common circuit mechanisms.

Micro-retinotopy in Orientation Maps

Previous electrode studies have indirectly assessed V1 micro-retinotopy by quantifying the degree of scatter in RF position for cells recorded during a given penetration (Dow et al., 1981; Hetherington and Swindale, 1999; Hubel and Wiesel, 1974; Van Essen et al., 1984). To directly characterize micro-retinotopy within maps of orientation preference, we used higher resolution two-photon imaging to measure responses of populations of individual neurons to a sparse-noise visual stimulus. The stimulus ensemble was parameterized for orientation and position (Figure 3), allowing us to extract each cell's orientation-tuning curve width and peak, along with its RF width and X/Y location (see Figure S1 for additional raw RF data). In Figures 4A and 4B, X and Y maps are plotted for four of our six imaging regions. To detect a retinotopic gradient at this cortical scale, the retinotopy must be precise; the depth of the gradient was expected to be small, given that V1 ($\sim 35 \text{ mm}$ across) was much larger than the imaged regions ($\sim 0.2 \text{ mm}$ across), but nonetheless greater than the magnitude of the positional scatter. From visual inspection, there appeared to be detectable gradients. To quantify the retinotopic precision, we first fit 2D planes to the X and Y position maps, which accounted for a significant amount of the variance (F -test, $p < 0.01$). The slope parameters also provided a

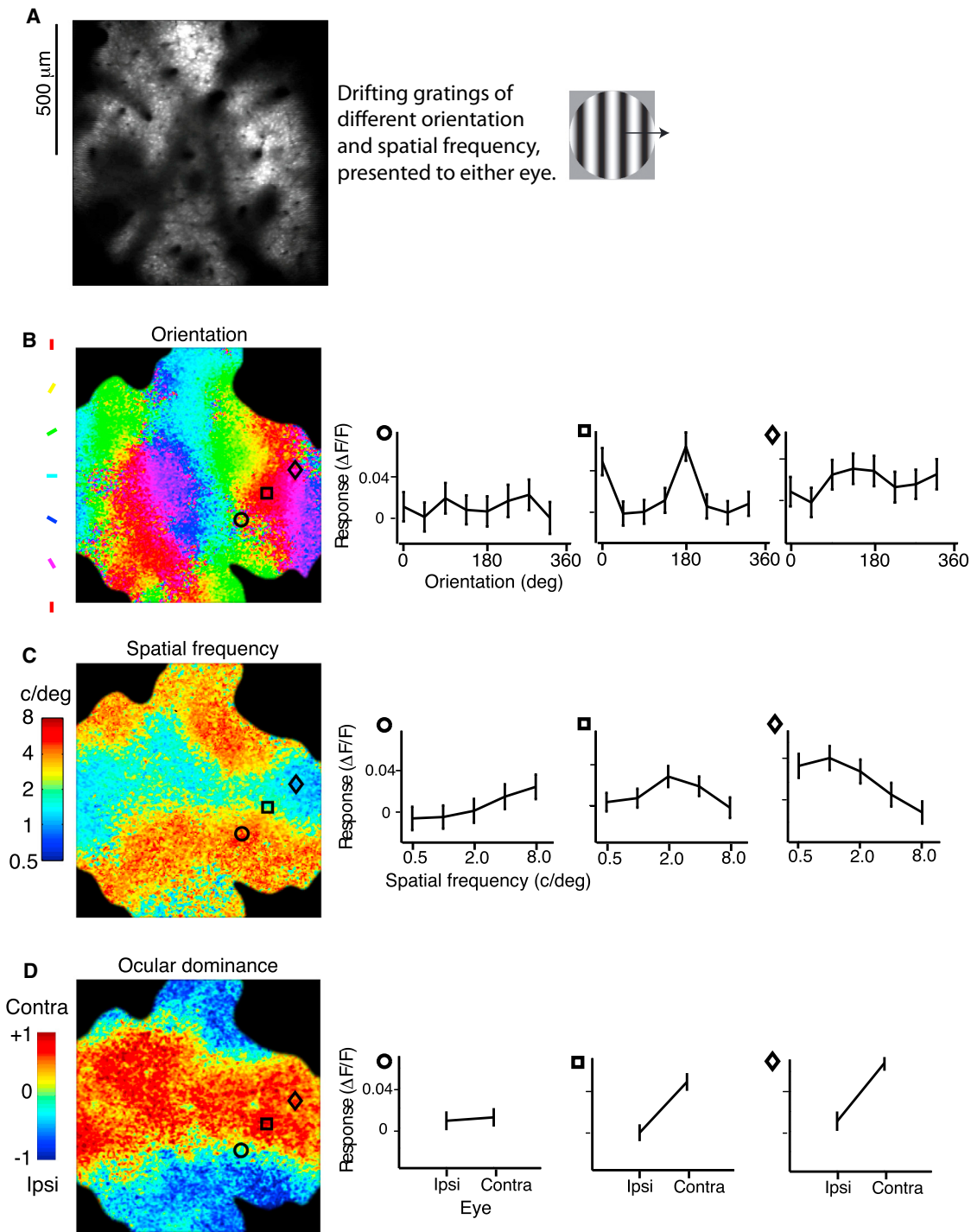


Figure 1. Computing the Preferred Orientation, SF, and OD at Each Pixel

(A) The average image from a single trial. Cells can be seen clearly in the image, but pixels are too large to determine the response of each cell independently of neuropil contributions. Drifting gratings of different orientation and SF were shown over the RFs for each eye.

(B) Orientation map. The preferred orientation at each pixel is computed from the tuning curves. The tuning curves from three pixel locations are shown to the right. SE bars were computed from variability across stimulus presentations.

(C) SF map. The color at each pixel represents the center of mass of the SF-tuning curve.

(D) OD map. Eye preference was computed by taking the response to the contralateral eye minus the response to the ipsilateral eye and dividing by the sum of both.

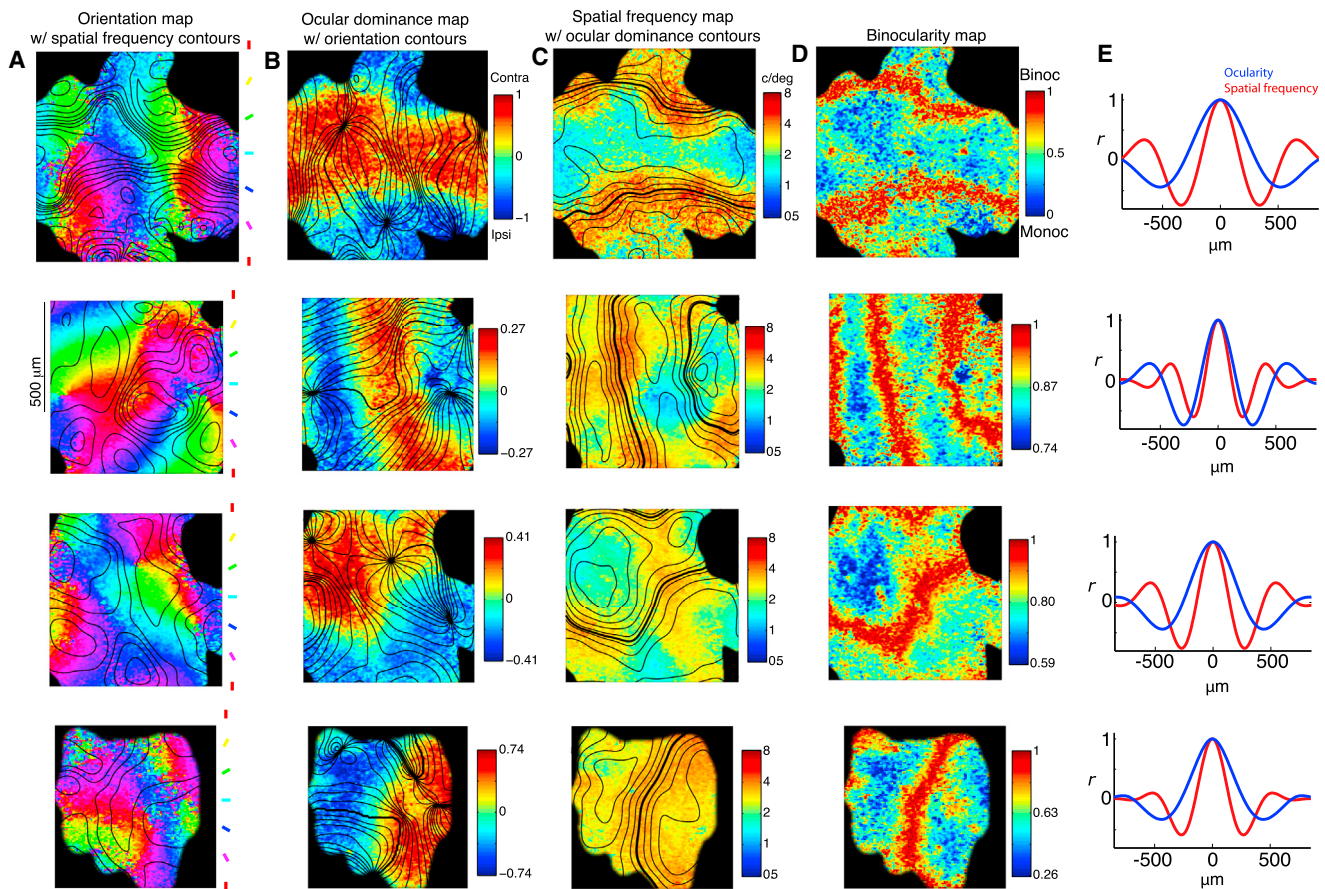


Figure 2. Relationships among Functional Maps

Each row is data from a single imaging region.

- (A) Orientation maps, with the iso-contour lines of the SF map in black. The SF contours are spaced 0.17 octaves apart.
- (B) OD maps, with iso-contour lines of the orientation map in black. Contours are spaced 10 degrees apart.
- (C) SF maps, with iso-contour lines of the OD map in black. The zero-crossing of the OD map is shown as a thicker contour line.
- (D) The binocularity map was computed as $1 - |\text{OD}|$.
- (E) Autocorrelation of OD and SF maps is projected perpendicular to the axis of maximum variance.

magnification factor for each imaging region ([Experimental Procedures](#), Equation 1), which was $0.47 \text{ mm}^2/\text{deg}^2$ and $5.90 \text{ mm}^2/\text{deg}^2$ for the first two regions of [Figure 4](#), the minimum and maximum of our six imaging regions ([Table 2](#)). This range is comparable to values measured on a coarser scale in parafoveal V1 ([Blasdel and Campbell, 2001](#); [Daniel and Whitteridge, 1961](#); [Dow et al., 1981](#); [Hubel and Wiesel, 1974](#); [Van Essen et al., 1984](#)).

To visualize the degree of RF scatter, we overlaid the RF contours of all neurons in each imaging region ([Figure 4C](#)). This qualitative assessment of the population was in stark contrast to previous studies ([Dow et al., 1981](#); [Hubel and Wiesel, 1974](#)), as the RFs were quite closely aligned without individual scatter. Next we computed a distribution of relative scatter for each imaging region as the deviation of an RF's position from the fitted planes, normalized by the RF width ([Experimental Procedures](#), Equation 2; [Figure 4C](#)). Mean relative scatter was between 0.11 and 0.17 in the six imaging regions ([Table 2](#)). With bulk-loaded calcium indicators like OGB, contamination of the measured neuronal responses by contribution from the neuropil

becomes a concern. We therefore assessed possible effects of neuropil contamination on the measurement of RF scatter, and we found it insufficient to explain the low relative scatter observed in our experiments (see the [Supplemental Experimental Procedures](#)). Small relative scatter implies that the point-image size can be computed based on magnification factor and average RF width alone ([Experimental Procedures](#), Equation 3). The computed point-image size (2σ) was between 0.91 and 1.26 mm in the six imaged regions ([Table 2](#)). This point-image size is ~ 2 -fold smaller than if relative scatter had a ratio of ~ 1 , as originally suggested ([Hubel and Wiesel, 1974](#)). For perspective, we note that the point-image is about $1/1,200^{\text{th}}$ the total area of V1, yet its width is slightly greater than the 1D spatial period of the OD maps.

Next we addressed the question of whether distortions in retinotopy, and thus distortions in the point-image, correlate with the orientation map. Previous studies disagree on whether changes in magnification factor correlate with transition zones in the orientation map ([Bosking et al., 2002](#); [Das and Gilbert,](#)

Table 1. Summary of the Alignment among Orientation, OD, and SF Maps

Imaging Region	Animal ID	Preferred Orientation/SF Intersection \angle (degrees)	Preferred Orientation/OD Intersection \angle (degrees)	Preferred SF/OD Intersection \angle (degrees)	r (SF versus $ \nabla OD $)	r (SF versus $1 - OD $)	SF Period (μm)	OD Period (μm)
u	1	86	82	2	0.50*	0.33**	690	1,140
v	2	82	62	23	0.28*	0.19**	430	630
w	2	63	85	16	0.28*	0.43**	580	960
x	2	83	78	25	0.18*	0.13**	590	990
y	3	81	87	14	0.41*	0.31**	596	600
z	4	86	89	28	0.19*	0.006	686	880

The first four (regions u–x) are shown in Figure 2 in the same order. First column: six patches of cortex were imaged, identified in each row as regions u–z. Second column: animal in which the region was recorded. Third column: the preferred intersection angle between the gradients of the orientation and SF maps (0–90 degrees). This is computed from the pixel-by-pixel distribution of intersection values. Fourth column: the preferred intersection angle between the gradients of the orientation and OD maps (0–90 degrees). Fifth column: the preferred intersection angle between the gradients of the SF and OD maps (0–90 degrees). Sixth column: correlation coefficient between $\log(\text{SF})$ and $|\nabla \text{OD}|$ across pixels. Seventh column: correlation coefficient between $\log(\text{SF})$ and $1 - |\text{OD}|$ across pixels. Only region z was not significant ($p > 0.05$). Eighth column: spatial period of the SF map (μm). Ninth column: spatial period of the OD map (μm). Note that the computed spatial period of the OD map is likely underestimated in instances where the imaged regions were smaller than the period of the map, thus yielding an underestimate of the ratio between the maps. For instance, region y had a ratio near unity, in spite of a significantly positive correlation between SF and the OD metrics. * $p < 10^{-10}$, ** $p < 0.05$.

1999; Hetherington and Swindale, 1999). To assess this relationship, we first computed a metric for RF independence between every pair of cells, defined as the distance between the two RF peaks divided by the sum of their widths (Experimental Procedures, Equation 4). RF independence was plotted against the absolute difference in orientation preference (Figure 4E), which yielded weak but significant correlations. However, this correlation may be a trivial consequence of pooling over cell pairs separated by a range of cortical distances (i.e., cell pairs separated by greater cortical distances are also more separated across the gradients of orientation and retinotopy maps). In a second analysis, we accounted for the gradients by using RF scatter instead of absolute RF peak position. We recomputed the pairwise RF independence after subtracting the planar fits of X and Y retinotopy from each RF location. There was no significant correlation between the orientation map and scatter in five of six imaging regions (Table 2). In summary, the map gradients can account for the correlation between retinotopy and orientation, which is a testament to the precision of the maps at this spatial scale.

Also notable from each imaging region of Figure 4 is the finding that many neuron pairs have non-overlapping orientation-tuning curves yet highly overlapping RF envelopes. This is highlighted in the maps obtained near the centers of orientation pinwheels (Figure 4, rows 2 and 3); there are an abundance of neuron pairs that respond to largely independent orientations (e.g., the points above the red tick on the y axis), yet these same pairs encode coincident retinotopic coordinates given that they are well below unity on the x axis. This shows that neurons are able to discriminate across a broad range of orientations within a localized coverage of visual space, which translates to effective orientation coverage within the point-image.

In summary, our measurements on retinotopic precision establish a point-image that is as small as possible, given the baseline constraints of RF size and magnification factor. Nonetheless, a given point-image encompasses sharp transitions in the orientation map to encode all orientations at each point.

DISCUSSION

Here we have used multiple scales of two-photon calcium imaging to answer fundamental questions about functional architecture and coding capacity in macaque V1. Our data show that primate V1 contains a smooth micro-retinotopy and achieves efficient coverage of orientation, OD, and SF within the retinotopy, using a combination of orthogonal and non-orthogonal map alignments. As expected from previous studies, OD and orientation maps were strongly orthogonal (Bartfeld and Grinvald, 1992; Obermayer and Blasdel, 1993), as were orientation and SF maps (Nauhaus et al., 2012). In contrast, we found that OD and SF maps have gradients that progress in parallel but have unique spatial periods, such that low SF coincides with the center of OD columns and high SF with binocular regions. Furthermore, by precisely examining retinotopy across V1 on a cell-by-cell basis, we observed systematic shifts of the RF centers that were much smaller than the RF widths. This imposes the need for the observed precise arrangement of functional maps to achieve efficient coverage of three different stimulus properties.

These observations have important implications for wiring precision within V1, and they provide new insights into how V1 converts thalamic lateral geniculate nucleus (LGN) inputs into a systematic representation of novel features that are extracted and transmitted to higher cortical areas. Because thalamic afferents lack tuning for the combinations of features (orientation, SF, and OD) that are represented and mapped within the more superficial cortico-cortical output layers, construction of the mapping relationships that we have observed must require cortical connections that are amazingly precise and highly organized. Consideration of how each of these features is represented and organized at each processing stage (thalamus, input layers, and output layers) and where new features are extracted and combined is therefore informative about how this is accomplished.

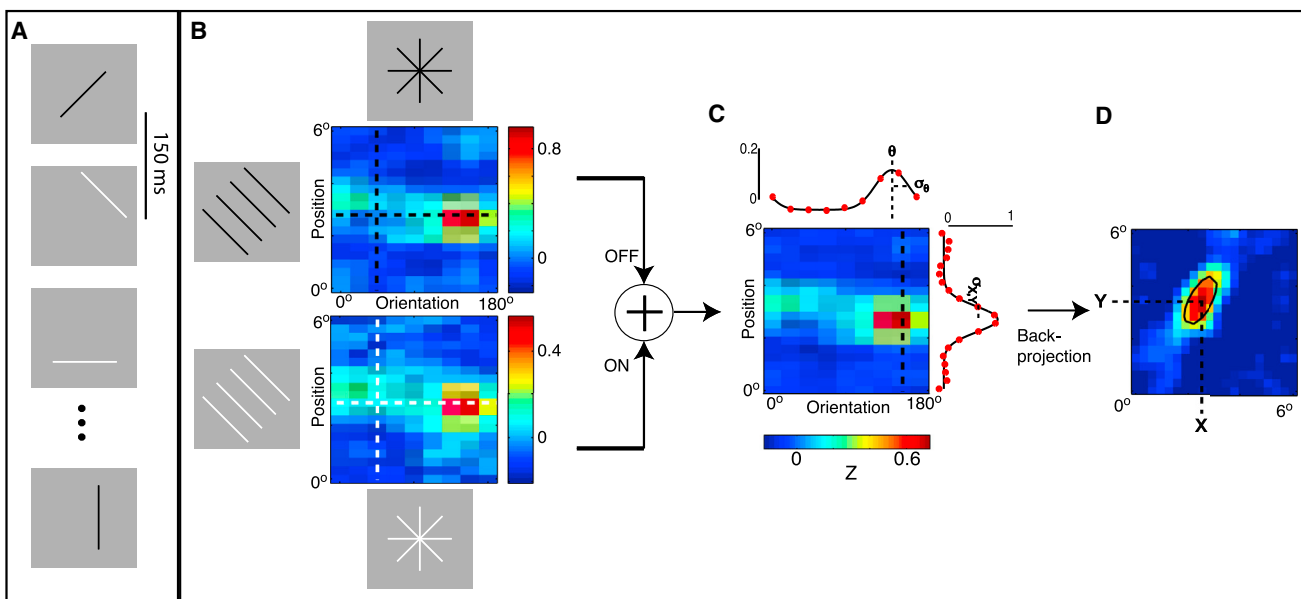


Figure 3. Constructing RFs from a Modified Sparse-Noise Stimulus

RF properties were measured from a sparse-noise stimulus.

- (A) Each presentation consisted of a static bar, randomized for orientation, position, and luminance.
- (B) For each neuron, the expected response to each orientation and position was taken at the optimal delay from stimulus onset. The response matrix of a single neuron is shown for the black (top) and white (bottom) bars. A vertical slice in the position-orientation matrix, shown by the vertical dashed line, is a series of aligned bars with the same orientation (left). A horizontal slice in the position-orientation matrix, shown by the horizontal dashed line, is a series of bars with different orientations that are the same radial distance from the center of the stimulus space (bottom and top).
- (C) Next the black bar and white bar response matrices were averaged together. Orientation-tuning curves were computed by taking the average over the position dimension (top, red dots) and fit with a Gaussian. Orientation preference and bandwidth were computed from the fits (top, black curve). To compute RF width, we first took a slice in the response matrix at the optimal orientation, which yielded the RF projection along the preferred orientation's axis (right, red dots). RF width was then quantified as 2σ from the Gaussian fit.
- (D) Lastly, the 2D RF profile was computed by performing back-projection on the orientation-position response matrix. After thresholding the kernel at the median, we fit a 2D Gaussian to identify the RF location in visual space. A contour line of the fit is overlaid in black.

Cortical Maps of Parallel Inputs

LGN inputs are monocular and un-oriented, so orientation selectivity and binocular features such as disparity tuning must be constructed within V1 and organized de novo into systematic maps. In contrast, LGN neurons are tuned for SF, and the three main parallel pathways provide broad coverage across the range of SFs: parvocellular neurons are tuned to the highest SFs, koniocellular are intermediate, and magnocellular are tuned to the lowest SFs (Derrington and Lennie, 1984; Irvin et al., 1993; Kaplan and Shapley, 1982). Thus, over the range of SFs represented in the LGN population, the observed smooth, systematic representation of SF maps in V1 can be created by simply mixing these three channels. Considerable evidence strongly suggests that this is done by a combination of organized thalamocortical and intracortical connections. It also appears that the organization of thalamic input contributes to the observed relationship between OD and SF, with lower SFs represented within monocular regions. Cytochrome oxidase (CO) blobs tightly align with the center of OD bands (Horton, 1984), and they receive a predominance of input from pathways that have larger RFs, koniocellular LGN afferents and magno-recipient layer 4C α (Callaway, 1998; Yabuta and Callaway, 1998a). Furthermore, blobs were shown to align with low-SF zones using electrophysiology (Born and Tootell, 1991; Edwards et al., 1995) and

2-[¹⁴C]deoxyglucose uptake (Silverman et al., 1989; Tootell et al., 1988). In contrast, the more binocular zones between CO blobs receive predominantly higher SF parvocellular inputs relayed from layer 4C β (Yabuta and Callaway, 1998a). While these studies point to differences between blob and interblob compartments, our data show that the transitions in both OD and SF tuning are gradual, consistent with anatomical evidence that long-distance connections linking columns treat transitions from blobs to interblobs as a continuum (Yabuta and Callaway, 1998b). Taken together, this study and others demonstrate a spatial coincidence among blob centers, the center of OD bands, low-SF zones, direct koniocellular input, and indirect magnocellular input, while the interblob zones demonstrate a similar relationship among binocularity, high SF, and parvocellular input.

Feedforward segregation of parallel inputs in macaque V1 helps explain the relationship between SF and OD maps, but it is less clear how parallel inputs might build orientation maps and their orthogonal alignment to SF and OD. The combined input from subcortical ON- and OFF-center pathways has long been recognized as the likely substrate for V1 orientation selectivity (Hubel and Wiesel, 1962). Studies in the carnivore have shown columnar biases of on-off polarity in geniculate afferents (Jin et al., 2008; McConnell and LeVay, 1984; Norton et al., 1985;

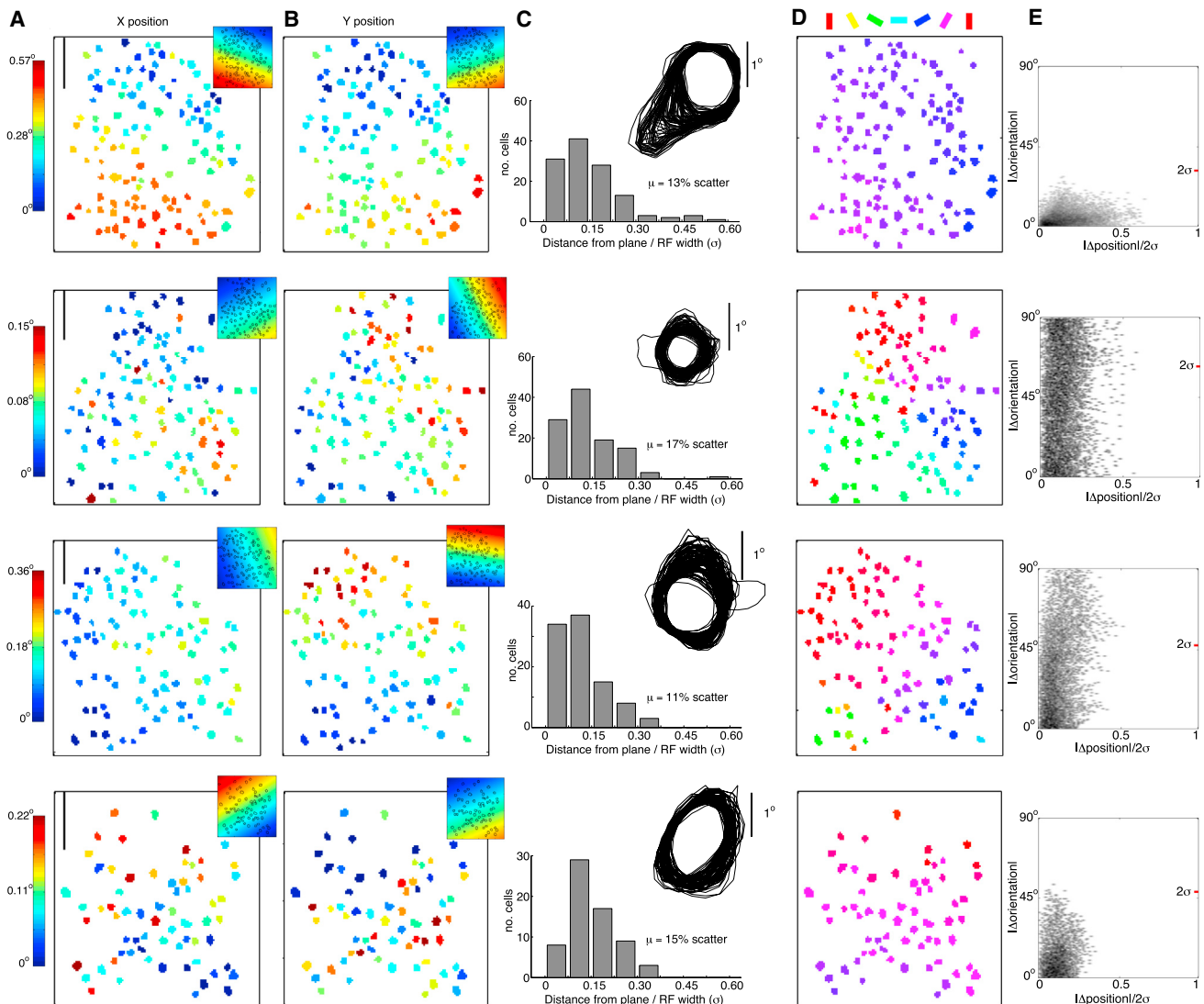


Figure 4. Micro-retinotopy within Maps of Orientation Preference

Each row is data from a single imaging region.

(A and B) Relative X (A) and Y (B) positions of each neuron's RF (in degree of visual angle) is color coded, with the corresponding planar fit in the top right corner. Planar fits accounted for a significant amount of the variance (F-test, $p < 0.01$). Scale bar at top left, 50 μ m.

(C) To quantify RF scatter, the residual error from the planar fits was normalized by RF size. Relative scatter was computed as the mean of the normalized residual error distribution. Half-height contour lines are an overlay of the RF profiles of all neurons in an imaging region.

(D) Color-coded orientation preference for each neuron is shown.

(E) Micro-retinotopy versus orientation map. Each data point is computed from a pair of neurons in the imaging region. The x axis denotes the absolute distance between the two RFs, normalized by the sum of their widths. The y axis denotes the absolute difference in preferred orientation. The red tick mark shows the average orientation tuning curve width as 2σ . A small but significant positive correlation was observed.

Smith et al., 2015; Zahs and Stryker, 1988) and V1 (Smith et al., 2015; Wang et al., 2015), which could be a scaffold for orientation maps (Jin et al., 2011; Kremkow et al., 2016; Lee et al., 2016; Miller, 1994; Paik and Ringach, 2011). It seems possible that OD and ON/OFF columnar biases are systematically aligned to produce the orthogonality between OD and orientation maps in the cat (Craig et al., 1997). Less is known about the horizontal organization of ON/OFF inputs to macaque V1, let alone the alignment between ON/OFF inputs and V1 maps

of orientation and OD. However, blue-ON afferents have patchy terminations in superficial V1 (Chatterjee and Callaway, 2003), which are likely koniocellular in origin, and may thus align with the OD columns. With additional data and modeling, the seemingly complex interdependences between maps and parallel inputs may begin to unfold and yield basic principles of connectivity. V1 maps provide a valuable constraint in addressing general questions about circuitry, regardless of their importance in cortical computation.

Table 2. Retinotopy Summary from Six Imaging Regions

Imaging Region	Animal ID	R_X^2	R_Y^2	RF Width (degrees) (2σ)	Scatter/ σ	$1/\ \nabla \hat{X}\ $ (mm/degrees)	$1/\ \nabla \hat{Y}\ $ (mm/degrees)	$ \angle \hat{X} - \angle \nabla \hat{Y} $ (degrees)	Magnification Factor ($\text{mm}^2/\text{degrees}^2$)	Point-image Size (mm)	$r(\Delta \text{Orientation}$ versus $\Delta \text{Pos}/\sigma)$	$r(\Delta \text{Orientation}$ versus $\Delta \text{Pos}/\sigma)$
a	5	0.69*	0.64*	1.30 ± 0.10	0.13	0.49	0.60	39	0.47	0.91	0.35**	0.01
b	6	0.18*	0.35*	0.54 ± 0.09	0.17	2.78	2.11	97	5.90	1.35	0.10**	-0.0002
c	7	0.51*	0.66*	1.08 ± 0.13	0.11	1.37	0.77	53	1.33	1.26	0.16**	0.009
d	6	0.34*	0.13	1.02 ± 0.12	0.15	1.05	-	-	-	1.07 ^a	0.13**	-0.0007
e	6	0.20*	0.27*	0.80 ± 0.06	0.17	1.60	1.37	88	2.20	1.22	0.08**	0.03
f	1	0.62*	0.34*	0.74 ± 0.07	0.16	0.85	2.63	126	2.78	1.26	0.22**	0.06*

The first four (regions a-d) are shown in Figure 4 in the same order. Second column: animal in which the region was recorded. Third column: R^2 of the fit of a 2D plane to the X-position retinotopy map. Fourth column: same for Y-position retinotopy map. Fifth column: average and SD of RF width (2σ), computed from a Gaussian fit along the axis perpendicular to the orientation preference. Sixth column: relative scatter, computed as the mean of the relative scatter distribution. Each point of the distribution is the RF's absolute distance from the X and Y planar fits, divided by the RF width (σ). Seventh column: the inverse of the maximum slope of the Y-plane fit. Eighth column: the angle of intersection between the gradients of the X and Y planar fits. Ninth column: the angle of intersection between the X and Y planar fit gradients. 11th column: point-image size, computed from RF width, magnification factor, and absolute scatter. 12th column: correlation coefficient between pairwise change in orientation preference and distance between RFs (normalized by sum of widths). 13th column: same pairwise comparison, but after subtracting the planar fits from the X and Y RF positions. *F-test p value < 0.01, **p < 0.01.

^aMagnification was computed only from the X-plane, as a significant fit was not identified for the Y-plane fit.

Binocular Disparity Tuning in V1

Binocular V1 neurons often exhibit disparity tuning, i.e., responses are maximized by a unique phase differential between images on the two retinas. Disparity tuning arises in V1 and is thought to represent the initial stage of depth perception in the visual cortex. SF selectivity and OD are particularly significant parameters in most models attempting to explain V1's disparity tuning. For instance, the disparity energy model predicts that high-SF-preferring cells should be more sharply tuned for disparity since they are able to detect finer changes in visual space. Electrode recordings have shown this to be the case, but the dependence is not particularly strong (Ohzawa et al., 1997; Prince et al., 2002; Smith et al., 1997). The energy model also predicts that the most binocular cells should have the strongest disparity discrimination. However, most experiments have shown that so-called monocular cells are actually tuned for disparity with a strength similar to binocular cells (Kara and Boyd, 2009; Kato et al., 1981; LeVay and Voigt, 1988; Ohzawa and Freeman, 1986; Poggio and Fischer, 1977; Prince et al., 2002; Read and Cumming, 2004; Smith et al., 1997). Taken together, the high-SF binocular zones we observed are not necessarily subpopulations of disparity encoders with the highest fidelity, as might otherwise be intuited. Further two-photon imaging of how disparity tuning intermingles with maps of orientation, SF, and OD within layer 2/3 (Kara and Boyd, 2009) may help to reconcile discrepancies and refine models of how disparity tuning arises in V1.

Comparison with Previous Measurements of Point-Image Parameters: RF Size and Scatter

The V1 point-image is directly relevant to V1's coding capacity, so it is not surprising that studies have modeled its size using estimates of RF size, RF scatter, and magnification factor (Equation 3). Our data indicate a smaller point-image than suggested by previous studies. The main source of discrepancy is the RF scatter: prior studies usually assumed larger RF scatter based on more indirect measures. Also, the measured RF size (and thus relative scatter and point-image size) can depend on the chosen visual stimulus. These issues are discussed in more detail below.

RF scatter has been the point-image dependency with the most uncertainty because of recording limitations. There are clear advantages of using two-photon imaging over electrodes to measure RF scatter. For one, many RFs can be measured at once, which provides statistical power and helps to account for changes in eye position that occur even in the anesthetized preparation. In other words, there is greater susceptibility to inflation of scatter from eye movements when single units are recorded successively over time. Second, relative cell locations can be determined precisely for all cells in the two-photon imaging region, which allowed us to account for the overall retinotopic gradient in estimating scatter. In summary, two-photon imaging yields parallel measurements of RFs of large populations, along with precise spatial localization of each cell. We believe these advantages have enabled our novel result of smooth micro-retinotopy in macaque V1.

Another potential source of contrast with prior studies is that scatter is greater in the deeper layers than what we have

reported in layer 2/3. Although we are not aware of any studies that have examined laminar dependencies of scatter, we can look to previous studies on laminar dependencies of RF size to help address this issue. For example, cells within layers 4A, 4C α , and 4C β have smaller RFs than cells in layers 4B and 5 (Blasdel and Fitzpatrick, 1984). The former layers would have greater relative scatter for the same retinotopic positioning of the RFs. Other studies have shown less dependency of RF size on V1 depth, aside from a preponderance of somewhat larger RFs in deeper layers (Angelucci et al., 2002; Cavanaugh et al., 2002; Hubel and Wiesel, 1977; Levitt and Lund, 2002). A study in V1 of the awake primate also reported that the mean size of RFs in layer 2/3 tended to be smaller than most other layers (Gur et al., 2005). The overall evidence therefore suggests that the RFs we are measuring in layers 2/3 tend to be on the smaller end of the spectrum. Therefore, prior studies suggest that relative scatter is unlikely to be significantly greater in deeper layers. Yet, the size of the point-image in these layers could be somewhat larger based on differences in RF size alone.

Finally, it is important to consider that V1 RF sizes, and thus the point-image, are stimulus dependent. The stimulus used here, randomized presentation of elongated bars, was designed to quickly yield quantitative measurements of V1 RFs for all cells in an imaging region. Our RFs can be classified as a minimum response field (mRF) (Barlow et al., 1967) and had widths between 0.5 and 1.3 degrees (Table 2). Earlier reports of mRF width tend to be smaller, between 0.2 and 1.0 degrees at a similar eccentricity (Blasdel and Fitzpatrick, 1984; Gattass et al., 1981; Hubel and Wiesel, 1974; Van Essen et al., 1984). However, these prior studies typically identified mRF qualitatively by periodically flashing small stimuli. Our more persistent presentation of oriented bars may put each cell in a response regime that is above the baseline average and, thus, more likely to drive the cell at the fringes of the RF. This effect would increase RF width, reduce relative scatter, and increase point-image size. Yet another method of measuring RF size is to determine the stimulus size, along a stimulus size-tuning curve, at which firing rate no longer increases (Angelucci et al., 2002; Cavanaugh et al., 2002; Kapadia et al., 1999; Levitt and Lund, 2002; Sceniak et al., 1999). Using this method in parafoveal V1, reported averages of RF size are \sim 1.0 degree, which are more similar to our measurements (i.e., larger) than the early mRF measurements. Considering that the size-tuning experiments used larger, steady-state drifting gratings, they are also more likely to drive the RF border and yield greater estimates of the RF and point-image size.

Advantages of Smooth Micro-retinotopy

Why would the V1 circuitry enforce such precise retinotopy? For one, a retinotopically organized circuit conserves space, time, and energy by performing local computations of the visual scene locally within the brain (Chklovskii and Koulakov, 2004). For instance, the RF overlap we have observed would allow the dense network of columnar connections to link neurons that process a localized region of the visual field. Next, RF scatter requires a complex untangling by downstream areas to fully decode V1's output. With precise retinotopy, new tuning properties in the visual hierarchy could instead arise from simpler mechanisms, e.g., homogenous pooling from non-homogenous

neighborhoods of the functional maps (Nandy et al., 2013; Nauhaus and Nielsen, 2014; Paik and Ringach, 2011). Lastly, smooth micro-retinotopy seems likely to enhance the perceptual discrimination of object shape and position by increasing spatial resolution. Multiple wide-field imaging studies have shown that shape and position discrimination are at least partly encoded within retinotopic coordinates of the V1 population response (Duncan and Boynton, 2003; Michel et al., 2013; Murray et al., 2006; Schwarzkopf et al., 2011). The resolution of this decoding mechanism would be limited by the size of the point-image.

Conclusions

Our two-photon imaging data demonstrate that the organization of the functional architecture in primate V1 is more rigid and stereotyped than previously thought, yet consistent with the original notion of the V1 hypercolumn. Primate behavior relies heavily on bottom-up visual information routed through superficial V1, a fact that has likely leveraged this organization. Future studies will need to assess exactly how the functional architecture, and thus neuronal tuning, is built from the similarly specific input and local V1 circuits (Callaway, 1998).

EXPERIMENTAL PROCEDURES

Animal Preparation and Surgery

All procedures were conducted in accordance with guidelines of the NIH and were approved by the Institutional Animal Care and Use Committee (IACUC) at the Salk Institute. We used a total of seven juvenile macaque monkeys in these experiments. Data for the retinotopy experiments are from four of the seven (one female *M. mulatta*, two male *M. fascicularis*, and one male *M. radiata*); data for the wide-field mapping also are from four of the seven (two male and one female *M. radiata* and one male *M. fascicularis*). Data from four of these animals also were used in a previous study (Nauhaus et al., 2012). Details of the experimental and surgical approaches are given in Nauhaus et al. (2012). Briefly, anesthesia was maintained throughout the experiment with sufentanil citrate (4–20 μ g/kg/hr, intravenously [i.v.]), supplemented with isoflurane (0.5%–2%) during surgeries. In a few cases, we additionally administered diazepam (50–100 μ g/kg, i.v.) as needed. For two animals, we used low levels of isoflurane (0.3%–0.5%) throughout the entire experiment. Animals were paralyzed with pancuronium bromide (0.1–0.2 mg kg $^{-1}$ hr $^{-1}$, i.v.) and artificially ventilated. The EtCO₂, electrocardiogram (EKG), electroencephalogram (EEG), SpO₂, heart rate, and body temperature were monitored continuously to judge the animal's health and maintain proper anesthesia levels. For imaging, we attached a custom-made well to the skull over V1. Eyes were dilated with 1% atropine and corneas were protected with contact lenses. External lenses refracted the eyes, with optimal refraction determined by the ability of V1 neurons to resolve fine spatial frequencies.

Multicell Bolus Dye Loading and In Vivo Two-Photon Microscopy

Injection of a dye solution containing OGB and sulforhodamine 101 (both Life Technologies), as well as the imaging, was performed as described previously (Nauhaus et al., 2012). Imaging was performed at 920-nm excitation and at two different spatial scales for micro-retinotopy and other feature maps. A 40 \times objective lens (0.8 numerical aperture [NA], Olympus) was used to assess micro-retinotopy, and a 16 \times objective lens (0.8 NA, Nikon) was used for imaging wide-field functional maps. Images were acquired at a frame rate of 16 Hz for the former and between 2 and 8 Hz for the latter. Eccentricity was at 6–10 degrees from the fovea, and depth was between 200 and 350 μ m below the cortical surface. We estimate that imaging regions in the micro-retinotopy experiments were approximately between 8 and 12 mm lateral (along the mediolateral (M-L) axis) from the midline, and imaging regions in the wide-field experiments were approximately between 10 and 15 mm. Data were collected with ScanImage software (Pologruto et al., 2003).

Visual Stimuli and Computing Tuning Curves

Visual stimuli were generated using the Psychophysics Toolbox extensions for MATLAB (Brainard, 1997; Pelli, 1997) on a 17-in cathode-ray tube (CRT) monitor ($1,024 \times 768$) with a refresh rate of 100 Hz. The monitor was gamma corrected using a Photo Research-701 spectroradiometer. The monitor was positioned at a distance of 60–80 cm from the animal.

Wide-Field Functional Maps

To measure orientation, SF, and OD, we computed responses of individual pixels to drifting gratings. Sinewave gratings were presented to one eye at eight directions (45-degree steps) and five spatial frequencies (0.5–8 cycles/degree spaced logarithmically) at full contrast. Stimulus size was ~30 degrees wide. Gratings were shown for 3 s on each trial, and a uniform gray screen was shown between trials. For three of the six imaged regions, the full set of sinewave gratings was randomly presented to either eye, from which OD could be assessed. For the three other imaging regions, the sinewave gratings were presented to only one eye. OD was assessed in a subsequent experiment, in which we presented square wave gratings fixed at 1.0 cycle/degree randomly interleaved across eight orientations and the two eyes. Six to seven repeats of each stimulus condition were always shown.

The response time course of each pixel for each trial was first computed as $[F(t) - F_0]/F_0$, where F_0 is the mean response to the gray screen prior to stimulus onset for the given trial. To compute each point of a pixel's tuning curve, we computed the average of $[F(t) - F_0]/F_0$ within the stimulus time window and across repeated presentations. Orientation preference was computed as $(1/2) \angle \sum_{\theta} T_{\theta} e^{j2\theta}$, where T_{θ} is the tuning curve as a function of orientation. SF preference was determined by first computing the center of mass (CoM) of the SF-tuning curve in the logarithmic domain, $\text{CoM}[T_{\log_2(\phi)}]$, followed by taking 2^{CoM} to put the metric in units of cycles/degrees. OD (contralateral versus ipsilateral eye) was measured as $(\text{contra} - \text{ipsi})/(\text{contra} + \text{ipsi})$. The mean of each OD map was subtracted.

For further analysis, the imaging region was cropped based on a signal-to-noise ratio (SNR) metric. The SNR of each pixel was computed at the time to peak of the average response to the best stimulus. SNR was measured as $(\mu_{\text{max}} - \mu_{\text{min}})/(\text{SE}_{\text{max}} + \text{SE}_{\text{min}})$, where μ_{max} and μ_{min} are the mean responses to the best and worst stimulus, and SE_{max} and SE_{min} are the corresponding SEs. Next this SNR image was smoothed with a 2D Gaussian ($\sigma = 25 \mu\text{m}$). The cropped region of interest (ROI) used for analyses consisted of pixels with $\text{SNR} > 2$. Areas of the map with $\text{SNR} < 2$ are darkened in the images (Figure 2).

Micro-retinotopy

To measure the micro-retinotopy, we computed responses of individual neurons to a sparse-noise stimulus presented monocularly. Following off-line movement correction (Nauhaus et al., 2012), time courses were extracted from the pixels of each neuron. Time courses were filtered with a difference of Gaussians ($\sigma_{\text{lowpass}} = 5 \text{ ms}$; $\sigma_{\text{highpass}} = 5,000 \text{ ms}$) and then Z scored within each 60-s trial. The visual stimulus consisted of static bars varying in orientation, position, and luminance, shown in succession every 100–200 ms (Figure 3). Prior to performing the additional computations described below, responses were averaged into eight to ten orientation bins and 20–30 position bins. Positional binning was spaced approximately at the bar's width (0.2–0.3 degrees) within the domain's range of 6–7 degrees. The bar's length was between 5 and 7 degrees. There were two luminances for each bar (black and white bars on a gray background). The average response kernel for orientation (θ), position (P), luminance (L), and time delay after stimulus onset (τ) is given as $K(\theta, P, L, \tau)$. Each kernel was taken at the time slice of maximum response to give $K(\theta, P, L, \tau_o)$ shown in Figure 3B. Because ON and OFF sub-fields were overlapping for most cells (i.e., $K(\theta, P, \text{white}, \tau_o) \sim K(\theta, P, \text{black}, \tau_o)$), responses to black and white bars were averaged to give $K(\theta, P, \tau_o) = K(\theta, P)$ (Figure 3C).

Multiple RF properties were then extracted from each neuron's spatial response kernel, $K(\theta, P)$. For each orientation of the stimulus domain, position varied along the orthogonal axis. In turn, responses to a given orientation yielded a 1D projection of the 2D RF. RF width was computed by fitting a 1D Gaussian at the slice of optimal orientation, $K(\theta_o, P)$ (Figure 3C, right). Next, an orientation-tuning curve was produced by summing the kernel over position, $\Sigma_P [K(\theta, P)]$, from which orientation-tuning width and preference were computed by fitting a 1D Gaussian (Figure 3C, top). To compute the 2D loca-

tion of the RF, we first performed back-projection on $K(\theta, P)$ to get the RF in Cartesian coordinates, $R(x, y)$. $R(x, y)$ was then thresholded at the median (Figure 3D), and finally it was fit with a 2D Gaussian to obtain a robust estimate of RF position.

Neuron selection for further analysis was based on the quality of the Gaussian fits. The exclusion of neurons can be seen explicitly in Figure 4. The upper-right insets of Figures 4A and 4B provide outlines for all neurons that were initially selected in the raw image; i.e., their selection was based solely on the anatomical identification of neuronal cell bodies in an image that was the average of one trial. The larger retinotopy maps of Figures 4A and 4B show the subset of neurons selected to analyze micro-retinotopy and relative scatter; we only used RFs with 2D Gaussian fits that accounted for 50% of the variance. At least 98% of the RFs in each of the six imaging regions passed this criterion. Next the analysis of orientation tuning versus retinotopy (Figure 4E) only used fits to the orientation tuning curves that accounted for 50% of the variance. Compare the orientation preference maps in Figure 4D to the insets of Figures 4A and 4B to see which cells were removed based on this criterion. At least 92% of the orientation-tuning curves in each of the six imaging regions passed this criterion.

Analysis of Wide-Field Functional Maps

Computing Autocorrelation and Spatial Period

First, the 2D autocorrelation of both $\log(\text{SF})$ and OD maps was computed by taking the Pearson correlation coefficient (r) for each spatial shift. Only the pixels within the SNR-defined imaging region (see above) were used to compute r . Next we took a 1D projection of both SF and OD autocorrelation matrices along the axis that produced the maximum 1D variance in the OD map. Specifically, to identify the axis of maximum OD variance, we took the projection of the OD map along a discrete set of axes (i.e., we computed the Radon transform of the OD map), and the variance of the projected 1D waveform was computed for each axis. We then went back to the 2D autocorrelation functions of OD and SF and computed the 1D projection along the same axis that yielded maximum variance in the OD map. Lastly, power spectra were computed from the Fourier transforms of the zero-padded (spatial padding interpolates in the spectral domain) autocorrelation, and the peak locations provided the spatial periods given in Table 1.

Gradient Intersection

The following steps were taken to compute the preferred intersection angle between map gradients (Table 1, columns 3–5). Orientation, SF, and OD maps were first smoothed with a 2D Gaussian ($\sigma = 9 \mu\text{m}$). Smoothing captures the trend of the gradient on the scale of the smoothing kernel. The gradient of the smoothed orientation map, $\nabla O_{x,y}$, was computed by taking the difference between values at adjacent pixels, followed by adding 180 to values <-90 degrees and subtracting 180 from values >90 degrees. The gradients of the smoothed SF map, $\nabla \log(\phi_{x,y})$, and OD map, $\nabla O_{x,y}$, were simply computed by taking differences between values at adjacent pixels.

Next the intersection angle between OD and SF maps was taken from the following resultant vector: $\vec{R} = \sum_k e^{j2[\Delta \nabla O_k - \Delta \nabla \phi_k]}$. The sum is over all pixels that are within the SNR-defined ROI. Note that Δ computes the axis of the gradient (i.e., yielding values in the range of 0 to 180 degrees). Finally, the preferred intersection angle equals $|(1/2) \angle \vec{R}|$, which gives a value in the range of 0 to 90 degrees when $\angle \vec{R}$ is defined in the range of -180 to $+180$ degrees. The intersection between orientation and SF, along with orientation and OD, was computed in the same manner.

Analysis of Micro-retinotopy

The RF position, $[X_i, Y_i]$, for each cell (i) was obtained from a 2D Gaussian fit, as described above. \hat{X} and \hat{Y} planes were then fit to each imaging region by linear regression. The slopes of \hat{X} and \hat{Y} yield a magnification as follows:

$$\text{Cortical magnification } \left(\frac{\text{mm}^2}{\text{deg}^2} \right) = \begin{vmatrix} \partial \hat{Y}/\partial u & \partial \hat{Y}/\partial v \\ \partial \hat{X}/\partial u & \partial \hat{X}/\partial v \end{vmatrix}^{-1}, \quad (\text{Equation 1})$$

which is the inverse of a determinant. u and v are the two dimensions on the cortical surface.

Relative scatter was computed for each imaging region as

$$\text{Relative scatter} = \left\langle \frac{\sqrt{(X_i - \bar{X}_i)^2 + (Y_i - \bar{Y}_i)^2}}{\sigma_{W,j}} \right\rangle_i, \quad (\text{Equation 2})$$

where the numerator is the absolute deviation of the RF's actual position from the fitted planes at the given cortical location (\bar{X}_i and \bar{Y}_i), the denominator is the RF's width at the preferred orientation (Figure 3C), and the brackets indicate that the ratio was averaged over all neurons.

By assuming that the RF envelope and the distribution of scatter are both Gaussian shaped, we can use the following equation to compute the size of the point-image:

$$\text{Point image size (mm)} = 2\sqrt{M[\langle \sigma_w^2 \rangle_i + \sigma_{\text{Scatter}}^2]} \quad (\text{Equation 3})$$

where M is the cortical magnification from Equation 1 and σ_{Scatter} is the average of the numerator in Equation 2. The point-image size is scaled to be 2σ of the Gaussian model.

To compare retinotopy with the orientation map, we first computed the following between each pair of cells, i and j :

$$\text{Receptive field independence} = \frac{\sqrt{(X_i - X_j)^2 + (Y_i - Y_j)^2}}{\sigma_{W,i} + \sigma_{W,j}}, \quad (\text{Equation 4})$$

where the numerator is the retinotopic distance between RF peaks, based on the 2D Gaussian fits, and the denominator is the sum of the RF widths, based on the 1D Gaussian fits at the optimal orientation. This was compared against the absolute difference in orientation preference (0 to 90 degrees) between the cell pairs (Figure 4E).

SUPPLEMENTAL INFORMATION

Supplemental Information includes Supplemental Experimental Procedures and three figures and can be found with this article online at <http://dx.doi.org/10.1016/j.neuron.2016.07.015>.

AUTHOR CONTRIBUTIONS

I.N., K.J.N., and E.M.C. designed the research, performed experiments, and wrote the paper. I.N. analyzed the data.

ACKNOWLEDGMENTS

This work was supported by NIH grant EY022577 and the Gatsby Charitable Foundation.

Received: January 16, 2016

Revised: April 13, 2016

Accepted: June 28, 2016

Published: August 4, 2016

REFERENCES

- Angelucci, A., Levitt, J.B., Walton, E.J., Hupe, J.M., Bullier, J., and Lund, J.S. (2002). Circuits for local and global signal integration in primary visual cortex. *J. Neurosci.* **22**, 8633–8646.
- Barlow, H.B., Blakemore, C., and Pettigrew, J.D. (1967). The neural mechanism of binocular depth discrimination. *J. Physiol.* **193**, 327–342.
- Bartfeld, E., and Grinvald, A. (1992). Relationships between orientation-preference pinwheels, cytochrome oxidase blobs, and ocular-dominance columns in primate striate cortex. *Proc. Natl. Acad. Sci. USA* **89**, 11905–11909.
- Blasdel, G., and Campbell, D. (2001). Functional retinotopy of monkey visual cortex. *J. Neurosci.* **21**, 8286–8301.
- Blasdel, G.G., and Fitzpatrick, D. (1984). Physiological organization of layer 4 in macaque striate cortex. *J. Neurosci.* **4**, 880–895.
- Born, R.T., and Tootell, R.B. (1991). Spatial frequency tuning of single units in macaque supragranular striate cortex. *Proc. Natl. Acad. Sci. USA* **88**, 7066–7070.
- Bosking, W.H., Crowley, J.C., and Fitzpatrick, D. (2002). Spatial coding of position and orientation in primary visual cortex. *Nat. Neurosci.* **5**, 874–882.
- Brainard, D.H. (1997). The Psychophysics Toolbox. *Spat. Vis.* **10**, 433–436.
- Callaway, E.M. (1998). Local circuits in primary visual cortex of the macaque monkey. *Annu. Rev. Neurosci.* **21**, 47–74.
- Cavanaugh, J.R., Bair, W., and Movshon, J.A. (2002). Nature and interaction of signals from the receptive field center and surround in macaque V1 neurons. *J. Neurophysiol.* **88**, 2530–2546.
- Chatterjee, S., and Callaway, E.M. (2003). Parallel colour-opponent pathways to primary visual cortex. *Nature* **426**, 668–671.
- Chklovskii, D.B., and Koulakov, A.A. (2004). Maps in the brain: what can we learn from them? *Annu. Rev. Neurosci.* **27**, 369–392.
- Crair, M.C., Ruthazer, E.S., Gillespie, D.C., and Stryker, M.P. (1997). Ocular dominance peaks at pinwheel center singularities of the orientation map in cat visual cortex. *J. Neurophysiol.* **77**, 3381–3385.
- Daniel, P.M., and Whitteridge, D. (1961). The representation of the visual field on the cerebral cortex in monkeys. *J. Physiol.* **159**, 203–221.
- Das, A., and Gilbert, C.D. (1999). Topography of contextual modulations mediated by short-range interactions in primary visual cortex. *Nature* **399**, 655–661.
- Derrington, A.M., and Lennie, P. (1984). Spatial and temporal contrast sensitivities of neurones in lateral geniculate nucleus of macaque. *J. Physiol.* **357**, 219–240.
- Dow, B.M., Snyder, A.Z., Vautin, R.G., and Bauer, R. (1981). Magnification factor and receptive field size in foveal striate cortex of the monkey. *Exp. Brain Res.* **44**, 213–228.
- Duncan, R.O., and Boynton, G.M. (2003). Cortical magnification within human primary visual cortex correlates with acuity thresholds. *Neuron* **38**, 659–671.
- Edwards, D.P., Purpura, K.P., and Kaplan, E. (1995). Contrast sensitivity and spatial frequency response of primate cortical neurons in and around the cytochrome oxidase blobs. *Vision Res.* **35**, 1501–1523.
- Gattass, R., Gross, C.G., and Sandell, J.H. (1981). Visual topography of V2 in the macaque. *J. Comp. Neurol.* **201**, 519–539.
- Gur, M., Kagan, I., and Snodderly, D.M. (2005). Orientation and direction selectivity of neurons in V1 of alert monkeys: functional relationships and laminar distributions. *Cereb. Cortex* **15**, 1207–1221.
- Hetherington, P.A., and Swindale, N.V. (1999). Receptive field and orientation scatter studied by tetrode recordings in cat area 17. *Vis. Neurosci.* **16**, 637–652.
- Horton, J.C. (1984). Cytochrome oxidase patches: a new cytoarchitectonic feature of monkey visual cortex. *Philos. Trans. R. Soc. Lond. B Biol. Sci.* **304**, 199–253.
- Horton, J.C., and Adams, D.L. (2005). The cortical column: a structure without a function. *Philos. Trans. R. Soc. B Biol. Sci.* **360**, 837–862.
- Hubel, D.H., and Wiesel, T.N. (1962). Receptive fields, binocular interaction and functional architecture in the cat's visual cortex. *J. Physiol.* **160**, 106–154.
- Hubel, D.H., and Wiesel, T.N. (1974). Uniformity of monkey striate cortex: a parallel relationship between field size, scatter, and magnification factor. *J. Comp. Neurol.* **158**, 295–305.
- Hubel, D.H., and Wiesel, T.N. (1977). Ferrier lecture. Functional architecture of macaque monkey visual cortex. *Proc. R. Soc. Lond. B Biol. Sci.* **198**, 1–59.
- Hübener, M., Shoham, D., Grinvald, A., and Bonhoeffer, T. (1997). Spatial relationships among three columnar systems in cat area 17. *J. Neurosci.* **17**, 9270–9284.
- Irvin, G.E., Casagrande, V.A., and Norton, T.T. (1993). Center/surround relationships of magnocellular, parvocellular, and koniocellular relay cells in primate lateral geniculate nucleus. *Vis. Neurosci.* **10**, 363–373.
- Issa, N.P., Trepel, C., and Stryker, M.P. (2000). Spatial frequency maps in cat visual cortex. *J. Neurosci.* **20**, 8504–8514.

- Jin, J.Z., Weng, C., Yeh, C.-I., Gordon, J.A., Ruthazer, E.S., Stryker, M.P., Swadlow, H.A., and Alonso, J.M. (2008). On and off domains of geniculate afferents in cat primary visual cortex. *Nat. Neurosci.* 11, 88–94.
- Jin, J., Wang, Y., Swadlow, H.A., and Alonso, J.M. (2011). Population receptive fields of ON and OFF thalamic inputs to an orientation column in visual cortex. *Nat. Neurosci.* 14, 232–238.
- Kapadia, M.K., Westheimer, G., and Gilbert, C.D. (1999). Dynamics of spatial summation in primary visual cortex of alert monkeys. *Proc. Natl. Acad. Sci. USA* 96, 12073–12078.
- Kaplan, E., and Shapley, R.M. (1982). X and Y cells in the lateral geniculate nucleus of macaque monkeys. *J. Physiol.* 330, 125–143.
- Kara, P., and Boyd, J.D. (2009). A micro-architecture for binocular disparity and ocular dominance in visual cortex. *Nature* 458, 627–631.
- Kato, H., Bishop, P.O., and Orban, G.A. (1981). Binocular interaction on monocularly discharged lateral geniculate and striate neurons in the cat. *J. Neurophysiol.* 46, 932–951.
- Kremkow, J., Jin, J., Wang, Y., and Alonso, J.M. (2016). Principles underlying sensory map topography in primary visual cortex. *Nature* 533, 52–57.
- Lee, K.-S., Huang, X., and Fitzpatrick, D. (2016). Topology of ON and OFF inputs in visual cortex enables an invariant columnar architecture. *Nature* 533, 90–94.
- LeVay, S., and Voigt, T. (1988). Ocular dominance and disparity coding in cat visual cortex. *Vis. Neurosci.* 1, 395–414.
- Levitt, J.B., and Lund, J.S. (2002). The spatial extent over which neurons in macaque striate cortex pool visual signals. *Vis. Neurosci.* 19, 439–452.
- McConnell, S.K., and LeVay, S. (1984). Segregation of on- and off-center afferents in mink visual cortex. *Proc. Natl. Acad. Sci. USA* 81, 1590–1593.
- Michel, M.M., Chen, Y., Geisler, W.S., and Seidemann, E. (2013). An illusion predicted by V1 population activity implicates cortical topography in shape perception. *Nat. Neurosci.* 16, 1477–1483.
- Miller, K.D. (1994). A model for the development of simple cell receptive fields and the ordered arrangement of orientation columns through activity-dependent competition between ON- and OFF-center inputs. *J. Neurosci.* 14, 409–441.
- Mountcastle, V., Berman, A.L., and Davies, P.W. (1955). Topographic organization and modality representation in first somatic area of cat's cerebral cortex by method of single unit analysis. *Am. J. Physiol.* 183, 646.
- Murray, S.O., Boyaci, H., and Kersten, D. (2006). The representation of perceived angular size in human primary visual cortex. *Nat. Neurosci.* 9, 429–434.
- Nandy, A.S., Sharpee, T.O., Reynolds, J.H., and Mitchell, J.F. (2013). The fine structure of shape tuning in area V4. *Neuron* 78, 1102–1115.
- Nauhaus, I., and Nielsen, K.J. (2014). Building maps from maps in primary visual cortex. *Curr. Opin. Neurobiol.* 24, 1–6.
- Nauhaus, I., Nielsen, K.J., Disney, A.A., and Callaway, E.M. (2012). Orthogonal micro-organization of orientation and spatial frequency in primate primary visual cortex. *Nat. Neurosci.* 15, 1683–1690.
- Norton, T.T., Rager, G., and Kretz, R. (1985). ON and OFF regions in layer IV of striate cortex. *Brain Res.* 327, 319–323.
- Obermayer, K., and Blasdel, G.G. (1993). Geometry of orientation and ocular dominance columns in monkey striate cortex. *J. Neurosci.* 13, 4114–4129.
- Ohzawa, I., and Freeman, R.D. (1986). The binocular organization of simple cells in the cat's visual cortex. *J. Neurophysiol.* 56, 221–242.
- Ohzawa, I., DeAngelis, G.C., and Freeman, R.D. (1997). Encoding of binocular disparity by complex cells in the cat's visual cortex. *J. Neurophysiol.* 77, 2879–2909.
- Paik, S.-B., and Ringach, D.L. (2011). Retinal origin of orientation maps in visual cortex. *Nat. Neurosci.* 14, 919–925.
- Pelli, D.G. (1997). The VideoToolbox software for visual psychophysics: transforming numbers into movies. *Spat. Vis.* 10, 437–442.
- Poggio, G.F., and Fischer, B. (1977). Binocular interaction and depth sensitivity in striate and prestrate cortex of behaving rhesus monkey. *J. Neurophysiol.* 40, 1392–1405.
- Pologruto, T.A., Sabatini, B.L., and Svoboda, K. (2003). ScanImage: flexible software for operating laser scanning microscopes. *Biomed. Eng. Online* 2, 13.
- Prince, S.J., Pointon, A.D., Cumming, B.G., and Parker, A.J. (2002). Quantitative analysis of the responses of V1 neurons to horizontal disparity in dynamic random-dot stereograms. *J. Neurophysiol.* 87, 191–208.
- Read, J.C., and Cumming, B.G. (2004). Ocular dominance predicts neither strength nor class of disparity selectivity with random-dot stimuli in primate V1. *J. Neurophysiol.* 91, 1271–1281.
- Sceniak, M.P., Ringach, D.L., Hawken, M.J., and Shapley, R. (1999). Contrast's effect on spatial summation by macaque V1 neurons. *Nat. Neurosci.* 2, 733–739.
- Schwarzkopf, D.S., Song, C., and Rees, G. (2011). The surface area of human V1 predicts the subjective experience of object size. *Nat. Neurosci.* 14, 28–30.
- Silverman, M.S., Grosos, D.H., De Valois, R.L., and Elfar, S.D. (1989). Spatial-frequency organization in primate striate cortex. *Proc. Natl. Acad. Sci. USA* 86, 711–715.
- Smith, E.L., 3rd, Chino, Y.M., Ni, J., Ridder, W.H., 3rd, and Crawford, M.L. (1997). Binocular spatial phase tuning characteristics of neurons in the macaque striate cortex. *J. Neurophysiol.* 78, 351–365.
- Smith, G.B., Whitney, D.E., and Fitzpatrick, D. (2015). Modular Representation of Luminance Polarity in the Superficial Layers of Primary Visual Cortex. *Neuron* 88, 805–818.
- Swindale, N.V. (1991). Coverage and the design of striate cortex. *Biol. Cybern.* 65, 415–424.
- Swindale, N.V., Shoham, D., Grinvald, A., Bonhoeffer, T., and Hübener, M. (2000). Visual cortex maps are optimized for uniform coverage. *Nat. Neurosci.* 3, 822–826.
- Tootell, R.B., Silverman, M.S., Hamilton, S.L., Switkes, E., and De Valois, R.L. (1988). Functional anatomy of macaque striate cortex. V. Spatial frequency. *J. Neurosci.* 8, 1610–1624.
- Van Essen, D.C., Newsome, W.T., and Maunsell, J.H. (1984). The visual field representation in striate cortex of the macaque monkey: asymmetries, anisotropies, and individual variability. *Vision Res.* 24, 429–448.
- Wang, Y., Jin, J., Kremkow, J., Lashgari, R., Komban, S.J., and Alonso, J.M. (2015). Columnar organization of spatial phase in visual cortex. *Nat. Neurosci.* 18, 97–103.
- Yabuta, N.H., and Callaway, E.M. (1998a). Functional streams and local connections of layer 4C neurons in primary visual cortex of the macaque monkey. *J. Neurosci.* 18, 9489–9499.
- Yabuta, N.H., and Callaway, E.M. (1998b). Cytochrome-oxidase blobs and intrinsic horizontal connections of layer 2/3 pyramidal neurons in primate V1. *Vis. Neurosci.* 15, 1007–1027.
- Yu, H., Farley, B.J., Jin, D.Z., and Sur, M. (2005). The coordinated mapping of visual space and response features in visual cortex. *Neuron* 47, 267–280.
- Zahs, K.R., and Stryker, M.P. (1988). Segregation of ON and OFF afferents to ferret visual cortex. *J. Neurophysiol.* 59, 1410–1429.